

## Research Article

# Wall Pressure and Blade Surface Pressure in a Side Channel Blower

Sven Münsterjohann  and Stefan Becker

Friedrich-Alexander-Universität Erlangen-Nürnberg, Cauerstr. 4, 91058 Erlangen, Germany

Correspondence should be addressed to Sven Münsterjohann; ms@ipat.uni-erlangen.de

Received 24 November 2017; Accepted 15 April 2018; Published 3 June 2018

Academic Editor: Jingyin Li

Copyright © 2018 Sven Münsterjohann and Stefan Becker. This is an open access article distributed under the Creative Commons Attribution License, which permits unrestricted use, distribution, and reproduction in any medium, provided the original work is properly cited.

In side channel blowers, the pressure field is the result of complex, inner flow mechanisms. While there are already experimental investigations on the wall pressure distributions, little is known about the pressure in the rotating system, i.e., on the blade surface. In this work, we present an experimental setup for measuring the unsteady blade surface pressure in several positions. The acquired data will be complemented by and compared to the additionally measured wall pressure on the side channel housing. Miniature pressure sensors are integrated into the impeller. It is modified to ensure flush mounted membranes of the sensors and to avoid impacting on the flow field. A telemetric system is used for a wireless transfer of the data from the rotating system to the data recorder. As a result, we show the time-resolved pressure distribution as well as its phase-locked ensemble average. The variations of the pressure field are related to the integral pressure difference across the turbomachine and to its rotational speed. Due to the high temporal resolution of the measurement data, an exact spatial localization of crucial flow phenomena is achieved. Low integral pressure differences show a nearly linear increase of the pressure in circumferential direction, while greater integral pressure differences evolve exponentially over the azimuth. The results confirm the circulatory flow theory. Different rotational speeds elicit a comparable behavior. The stripper is a dominant source for pressure fluctuations. Its individual geometric discontinuities are correlated to the flow field. Our results provide a deeper understanding of the flow phenomena in side channel blowers and the theory of pressure generation. Although the measurements were performed for only one type of side channel blower with a double-flow configuration and open blades, the energy transfer mechanism is the same for other modifications like single flow or closed blade versions.

## 1. Introduction

Side channel blowers close the gap between the classical turbomachines, like axial and radial fans, and the displacement pumps [1]. To characterize the operating point of turbomachines, two basic parameters are commonly used: the flow coefficient

$$\varphi^* = \frac{\bar{c}_C}{u} \quad (1)$$

is based on the rotational velocity at the blade tip  $u$  and the average velocity of the fluid in circumferential direction  $\bar{c}_C$  and the pressure coefficient

$$\psi^* = \frac{2Y_p}{u^2} \quad (2)$$

is based on the specific polytropic work  $Y_p$ . With tip speed ratios

$$\sigma^* = \varphi^{*^{1/2}} \psi^{*-3/4} \quad (3)$$

of  $5 \times 10^{-3} \dots 1 \times 10^{-1}$  and diameter numbers

$$\delta^* = \psi^{*^{1/4}} \varphi^{*-1/2} \quad (4)$$

of  $5 \dots 5 \times 10^1$ , side channel blowers are able to deliver comparably high heads while maintaining moderate flow rates. The cause is a complex 3-dimensional inner flow field. The highly turbulent flow field dissipates a rather large portion of the transferred energy [2]. Hence, the fluid temperature difference between suction port and outlet port can rise above values of 100 K [3]. Consequently, the polytropic efficiency does not reach values higher than  $\eta = 0.5$  [2, 3].

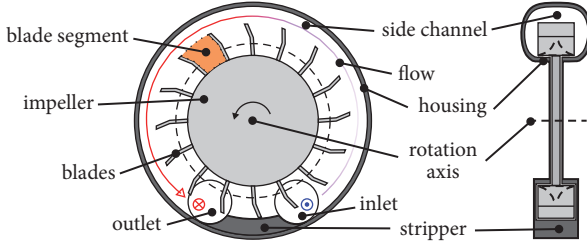


FIGURE 1: A double-flow side channel blower with radial, open blades.

The flow field is driven by the momentum transfer from the impeller to the fluid. Due to its simple design, the fluid particles can pass the impeller section multiple times and, hence, increase the momentum transfer as well as the resulting pressure. The suction port and the outlet port are separated by a stripper. It forms a geometric constriction with minimal gaps between the housing and the rotating impeller to ensure contact-free operation. A schematic drawing of a double-flow side channel blower is given in Figure 1.

The circumferential flow speed in the side channel is lower than the flow speed of the fluid between the blades. Hence, a fluid element located in the rotating region is accelerated in positive radial direction by the centrifugal acceleration. When it leaves the impeller, energy and momentum are transferred from this faster fluid element to the slower fluid in the side channel. Accordingly, new fluid from the side channel is sucked into the impeller near the hub. This flow theory is called circulatory flow theory and is widely discussed in literature [4, 5]. Depending on the number of blade passages, pressure is gained while the fluid moves in circumferential direction. A lower flow speed in the side channel results in a stronger deceleration of the circulating fluid and, hence, allows for more blade passages resulting in a higher pressure difference.

Based on this basic behavior, many analytical-empirical models have evolved. They account for the momentum transfer and the losses and allow estimating the pressure rise. Early models already included pressure losses of the circulatory flow [5–7]. Sixsmith and Altmann [8] investigated a side channel blower with aerodynamic blades in a theoretical and experimental manner. In [9] the influence of the stripper gap was analytically modeled and verified by experimental data revealing that the gap distance has an inverse effect on the efficiency. In [10] further analytical investigations related to the losses in regenerative turbomachines showed that the friction losses are the cause of the typically low efficiency. Grabow and Suong [11] used their analytical model to show the dependency of the head in correlation to the inlet and outlet blade angle. Further analytical approaches were derived in [12–15]. An innovation in the adoption of analytical models was introduced in [16] by taking into account the compressibility of the fluid.

Another flow theory, the mixing or turbulence theory, states that the momentum transfer is induced by the shearing or turbulent mixing of the fluid in the side channel and

the fluid between the blades [17–19]. The impeller is seen as a rough, moving wall, boosting the fluid in its immediate neighborhood to circumferential speed. However, this approach cannot explain the high heads side channel blowers are capable of delivering.

A comparison of both theories has been performed in [20]. The results show that the circulatory flow theory is superior to the mixing or turbulence theory in the explanation of the pressure generation in side channel blowers. The authors used computational fluid dynamics (cfd) simulations of a simplified and straightened side channel with an artificial momentum term to evaluate the effectiveness of both flow theories.

Numerical simulations of the flow field in side channel blowers show that a circulatory flow is established [21–23]. Even though numerical simulations allow for detailed insights into the flow field, few sources give a description of the spatial and temporal pressure field.

A detailed review of different aspects, i.e., operation, losses, and possible geometry and design optimizations is given in [24].

In [2, 3], Surek performed an analysis of the wall pressure field at eight different measurement positions. He showed that for a pressure side throttling configuration an increase of the volume flow results in a lower pressure and a lower temperature in the inlet region. Furthermore, his measurements revealed a nonlinear rise of the pressure in circumferential direction. Time-resolved measurements characterized the amplitude and frequency of the pressure oscillations in the side channel.

There are no international publications that experimentally examine the pressure field on the blade surface of a side channel blower under operation. Only Surek measured the blade surface pressure in [25, 26]. In his first setup, Surek used three miniature pressure sensors that were mounted onto the blades. The second setup consisted of four pressure sensors allowing for a higher spatial resolution. Describing the telemetry system in detail, he did not show how the integration of sensors was realized. From the information provided, the sensors seem to be mounted on the blade, creating an obstacle and disturbing the flow field. Nonetheless, the results give an insight into the dynamic behavior of the pressure field, especially during the stripper passage. Compression shocks during the blade segment closing and opening in the stripper region were identified. As the geometry of the stripper is not described, a reliable linkage to the observed flow effects is not available.

Analytical methods as well as cfd simulations allow calculating the pressure field in the side channel. In order to achieve a holistic representation of the fluid dynamic effects and to validate the preceding subjects, experimental data of the pressure field is essential.

This paper addresses the description of the pressure field in side channel blowers on the housing and the blade surface. It links the dominant pressure fluctuations to the geometric discontinuities caused by the stripper which is described in detail.

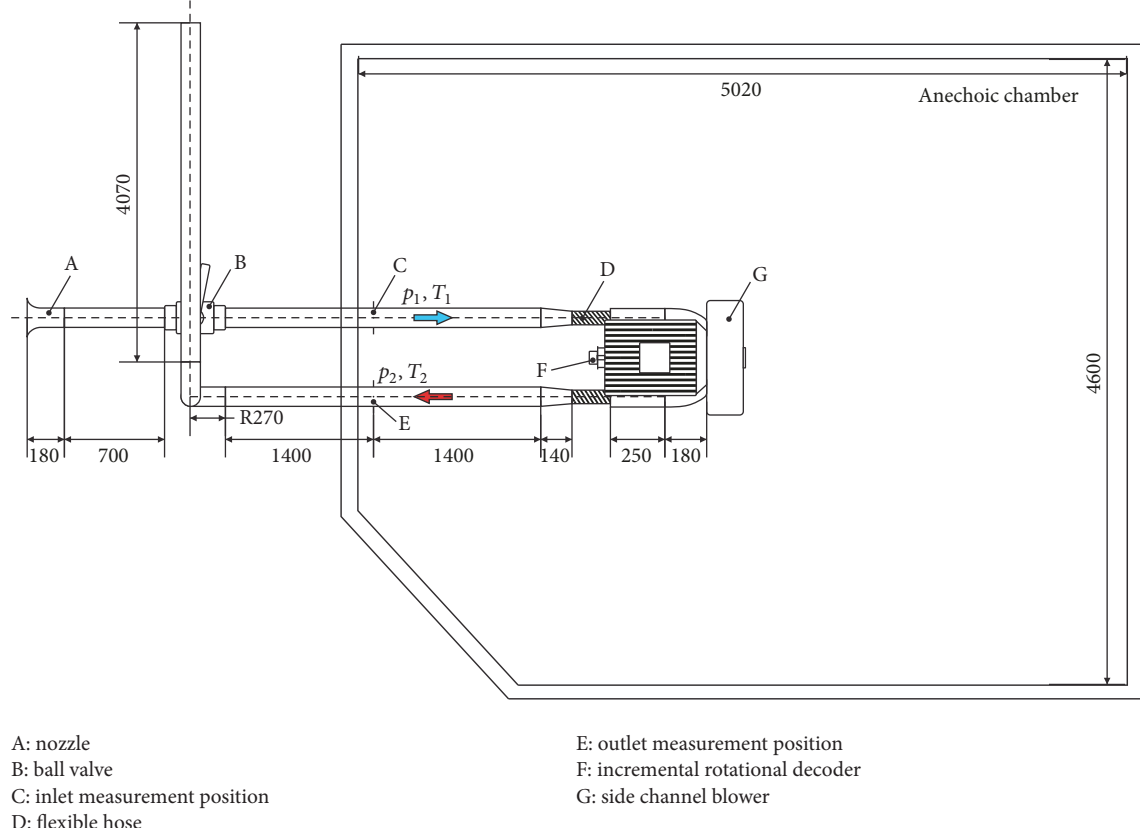


FIGURE 2: Basic experimental setup.

## 2. Materials and Methods

This section is divided into three parts: the basic setup for characterizing the hydraulic properties, i.e., volume flow rate, integral pressure difference, and rotational speed and the setups for wall pressure measurements on the blade surface and on the side channel wall. The measurements were performed with a side channel blower that has an outer diameter of 356 mm. The impeller has 55 blades and an outer diameter of 340 mm. The blade width is 45.9 mm and the blade height is 40.6 mm. The side channel blower has a double-flow configuration, forward-skewed radial blades, and a constant side channel cross section.

**2.1. Basic Experimental Setup.** As the setup is also used for acoustic measurements, which are not part of this work, the side channel blower (G) is located in an anechoic chamber as illustrated in Figure 2. The volume flow rate is computed from the pressure loss over a nozzle with an inner diameter of 80 mm (A) according to DIN EN ISO 5801. Further downstream, a ball valve (B) is used for suction side throttling. The pipe diameter is 65 mm. In a distance of 2.2 m in front of (C) and behind (E) the side channel blower, temperature and static pressure relative to ambient pressure are measured. The vibrational transmission between the pipe system and the side channel blower is decoupled by flexible hoses (D). An incremental rotational decoder (F) with a maximum resolution of 0.09° is mounted on the shaft of the

electric drive. It gauges the rotational speed and the azimuthal location of the impeller. Its signal was acquired with 250 kHz at 50 Hz rotational speed. The hot exhaust gas was discharged out of the chamber to ensure a constant inlet temperature. Temperature was measured using thermocouples of type K. The pressure in the inlet nozzle was measured with two differential pressure sensors from Setra type D239, one with a range of ±125 Pa and the other with a range of ±1245 Pa. We used sensors with different ranges to ensure a proper acquisition of the pressure loss for all working points. One connection of each sensor was attached to the nozzle; the other one was exposed to environmental pressure.

In order to minimize the environmental influence on the characteristic curves, the reduced pressure difference was calculated as follows [27]:

$$\Delta P_{12,\text{red}} = p_{\text{sc}} \left[ 1 - \left( \frac{T_1}{T_{\text{sc}}} \left[ \left( \frac{p_2 + \dot{V}_1^2 p_1^2 T_2 / 2A_p^2 p_2 R_s T_1^2}{p_1 + p_1 \dot{V}_1^2 / 2R_s T_1 A_p^2} \right)^{(n-1)/n} - 1 \right] + 1 \right)^{(n/(1-n))} \right] \quad (5)$$

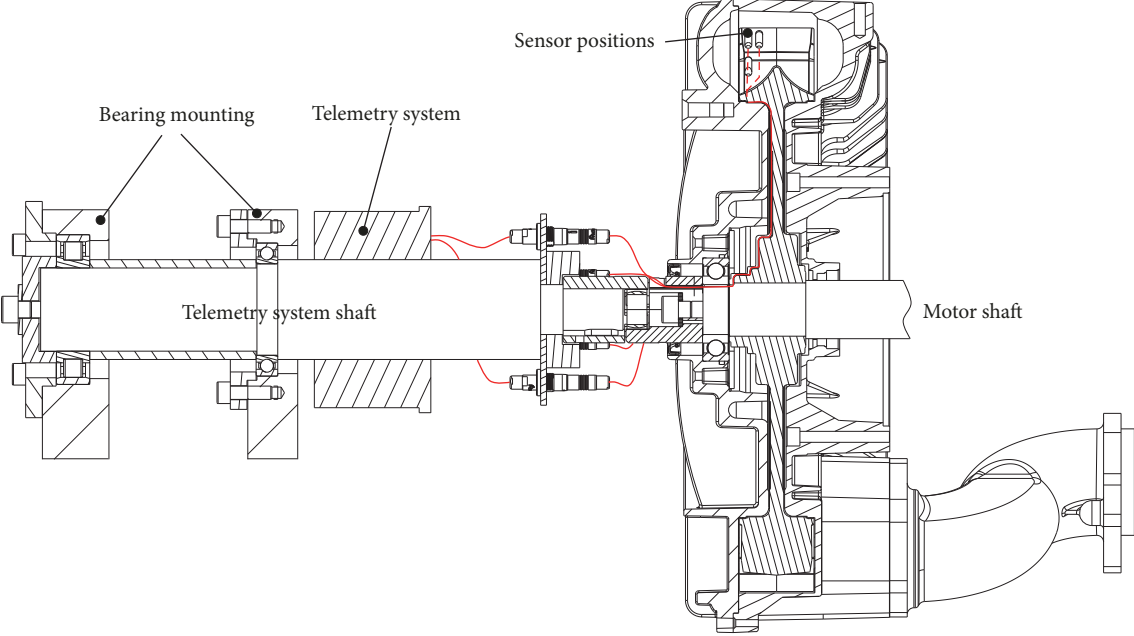


FIGURE 3: Setup for pressure measurements on the blade surface (support frame, motor, and balancing bodies not shown) with sensor cables in red.

with the atmospheric pressure for standard condition being  $p_{sc}$ , the inlet temperature  $T_1$ , the outlet temperature  $T_2$ , the corresponding absolute static pressures  $p_1$  and  $p_2$ , the temperature for standard condition  $T_{sc}$ , the specific gas constant for air  $R_s$ , the polytropic exponent  $n$ , the inlet pipe cross section  $A_p$ , and the volume flow rate at the inlet  $V_1$ .

For the measurement of a working point, the rotational speed of 50 Hz or 60 Hz and the desired pressure difference is set. Due to the dissipative effects, the fluid temperature rises and the pressure difference drops slightly. Therefore, the throttle is adjusted to meet the desired operating point. This iterative process is repeated until the outlet temperature and the operating point have converged.

**2.2. Blade Surface Pressure.** The greatest challenge in performing measurements on a rotating object is the power supply to and data transfer from the sensors. We used a telemetry system that allows for contactless operation. Figure 3 shows the described setup. A stator antenna surrounds the rotating antenna that directly performs the A/D-conversion. The latter is mounted on a shaft that is connected to the motor shaft with a claw coupling. Ensuring proper alignment of both shafts, the telemetry system shaft is driven by the motor. The side channel housing was modified by cutting a centric hole for the claw coupling to allow for this type of setup.

As the pressure sensors had to be flush mounted onto the blade surface, little cavities were eroded into blades, to house the sensors. After the installation, the cavities, except for the sensor membranes, were covered with a ultrathin, high-tensile steel sheet; see Figure 4. This way, we ensured that the flow field is not disturbed by any modifications. The locations of the sensor membranes are shown in Figure 5. Two impellers were used to be able to examine more positions.

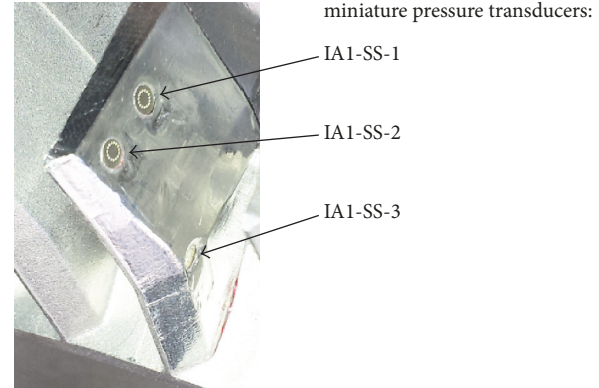


FIGURE 4: Flush mounted pressure transducers in blade (labels according to Figure 5).

Impeller arrangement 1 (IA1) has three sensors on each side of the blade on the streamline path according to the circulatory flow theory. The second impeller arrangement (IA2) covers the remaining area of the blade. Both impellers include a sensor on a reference position (**R**) for comparison. This results in a total number of 13 different sensor positions. The sensors are high temperature thin line pressure transducers Kulite LE-080 with a maximum calibrated temperature of 235°C and a size of  $9.6 \times 4.1 \times 1.5 \text{ mm}^3$ . Their natural frequency of 240 kHz is 24 times higher than the maximum frequency of interest. The sensors work in sealed gauge mode, which means that they hold an encapsulated reference pressure which is approximately the environmental pressure. The wires went through a hole to the neighboring blade segments, from where they were installed in a milled channel along the

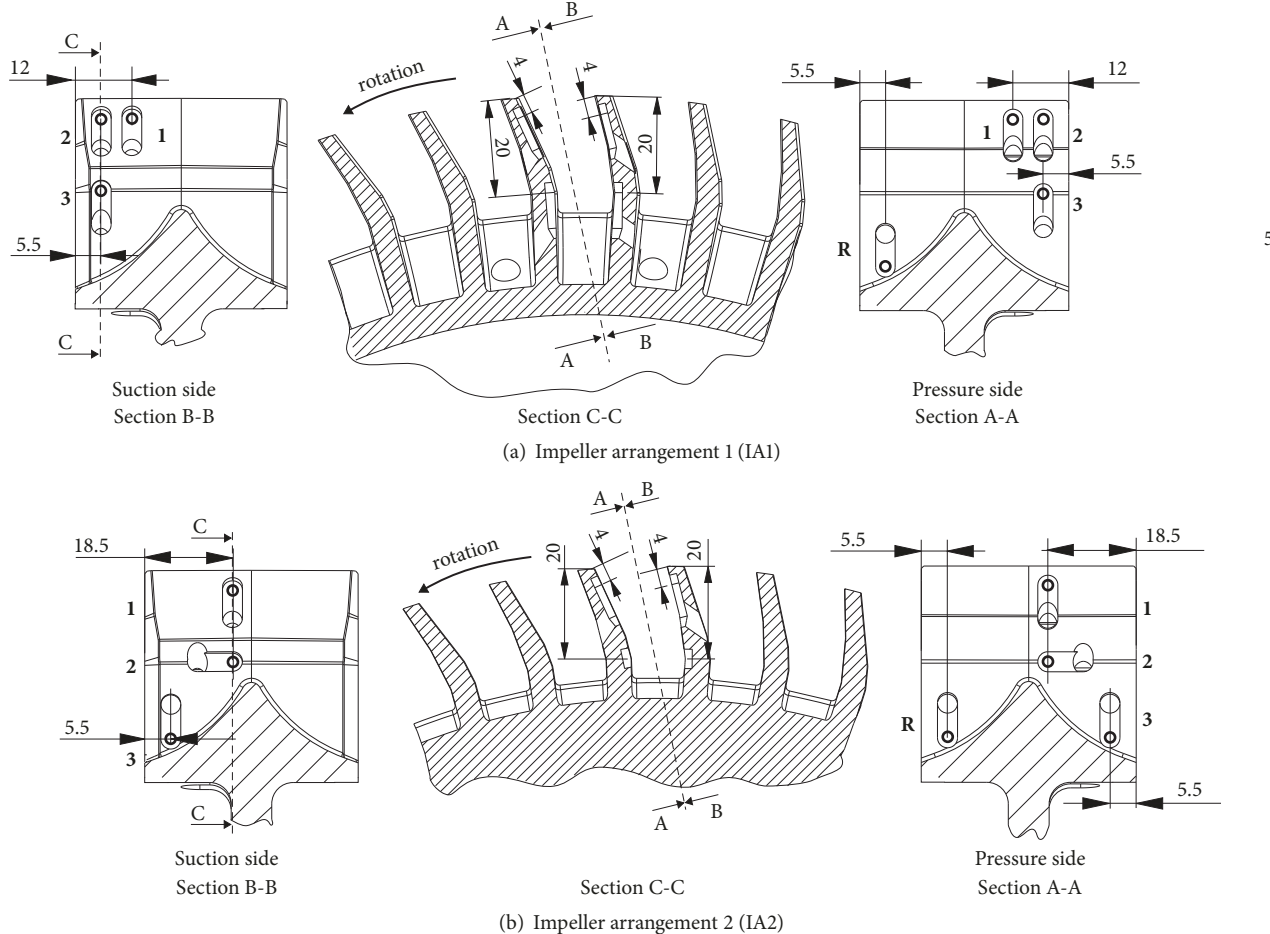


FIGURE 5: Positions of the pressure sensors (membrane position denoted by a black thick framed circle) in both impeller arrangements. Section B-B: view on suction side of the blade (SS); Section A-A: view on pressure side of the blade (PS). Sensor name in **bold**: example: impeller arrangement 1 (a) suction side of blade (left figure); Position 2 (sensor in the upper left corner of the blade): IA1-SS-2.

impeller hub. A modification of the shaft allowed a mounting of cables underneath the bearing. The cables then emerged through the claw coupling and contacted the rotor antenna, as shown in Figure 3.

The signals of the pressure sensors are acquired synchronously with a sampling rate of 100 kHz. This obviously high sampling rate was necessary to properly resolve the time trends of pressure changes in the region of the stripper. These effects occur at the blade passing frequency and are consequently resolved with 36 samples for a rotational speed of 50 Hz. We use a bridge module from National Instruments type PXIe-4431 with a maximum sampling frequency of 102.4 kHz for the acquisition. Transformations to the frequency domain were performed using the power spectral density (PSD) with a Hanning window and 50% overlap. By triggering both systems, the telemetry system and the data acquisition system for all other sensors, a common time base is ensured. When performing a measurement, the side channel blower operation is stopped after reaching temperature convergence. Then, the offset pressure of the sensors due to temperature and mechanical stresses is measured. Afterwards the side channel blower is set back to operation. This allows

for later correction of the measured pressure values during operation. The centrifugal acceleration induces a maximum worst case offset of approx. 1000 Pa into the measurement signals.

**2.3. Wall Pressure.** The unsteady wall pressure is measured using high temperature, cylindrical miniature pressure sensors with diameter of 2 mm, type Kulite XCE-080, working in differential mode. These sensors have also been flush mounted using a double sealing setup as shown in Figure 6. The natural frequency is typically 400 kHz, which is 40 times higher than the maximum frequency of interest.

The ten sensors were gradually located at four circumferential position (Pos. 1–4), each one resembling a cross formation; see Figure 7 depicted as “Unsteady measurem. pos”. The positions of the sensors were changed while the operating point was fixed and the side channel blower was operating. The remaining measurement positions were sealed from the outside using flush-mount plugs to avoid any change in the flow field.

The steady wall pressure was, additionally, acquired using a 64-channel measurement system (Pressure Systems DTC

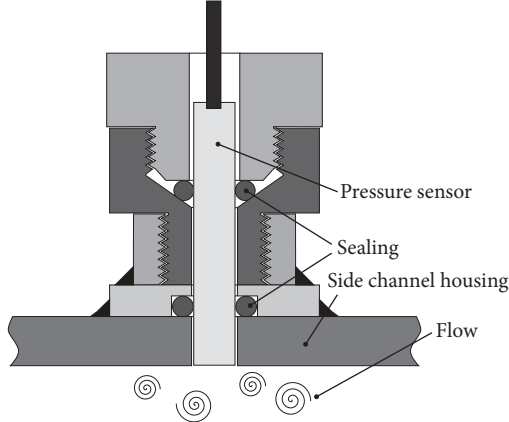


FIGURE 6: Wall pressure sensor mount.

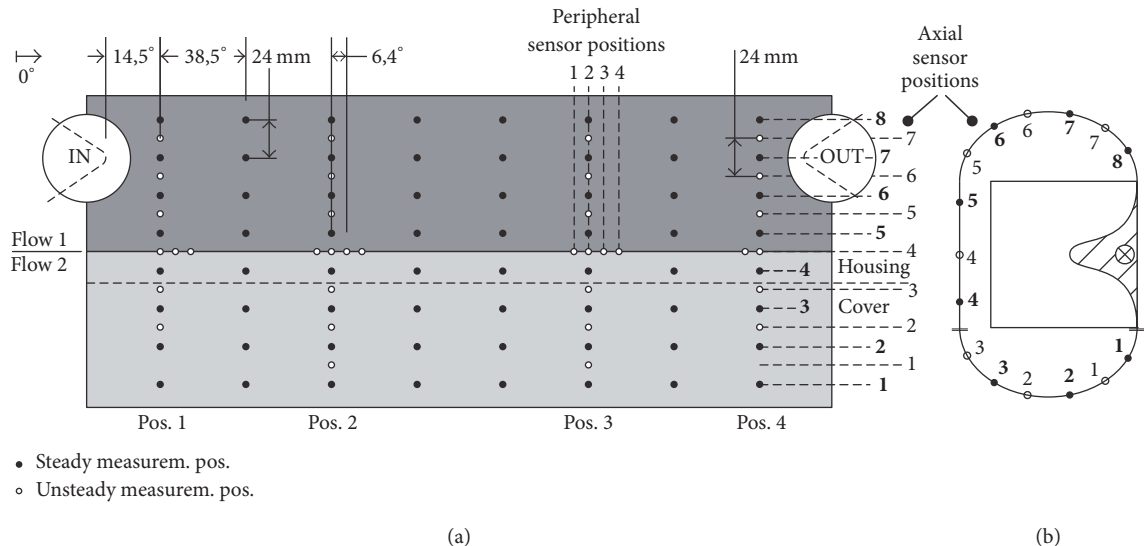


FIGURE 7: Measurement positions for wall pressure measurements: unwrapped side channel (a), axial cut (b).  $\varphi = 0^\circ$  is located in the middle of the stripper. First column of measurement positions (Pos. 1) is located at an absolute angle of  $45.1^\circ$ . Axial sensor positions marked with bold numbers depict steady measurements positions of the Pressure Systems DTC Initium. Axial sensor positions marked with normal numbers depict unsteady measurements positions of the Kulite pressure transducers.

Initium). The 64 measurement positions were equally distributed in circumferential and axial direction as shown in Figure 7 depicted as “Steady measurem. pos”. The sampling rate of the system is approx. 330 Hz. Hence, it only allows for steady analysis of the measurement data.

**2.4. Limitations.** The sensors in the rotating system are exposed to temperature variations and mechanical stresses. Both effects can lead to an offset of the measured, average pressure. These issues have been addressed by reducing the impact on the measured signal as much as possible by correcting the temperature-converged zero shift of the sensors as described above. Differences of the correction value to the operational mode are possible as the side channel blower had to be stopped for the zero-shift measurements.

Additionally, a pressure sensor integrated into the impellers is influenced by the centrifugal acceleration, but this offset does not change given a constant rotational speed. Also, the sensors are mounted in an almost circumferential direction; by that, the direction of the membrane that exhibits the smallest sensitivity is exposed to the resulting centrifugal force.

Furthermore, the results only show the pressure at discrete points and represent a surface or wall-bound view of the pressure field. Hence, the locally measured pressure includes, for example, stagnation effects and does not resemble a 3-dimensional representation of the pressure field distant from the side channel surface.

Three different measurement systems were used that were synchronized offline by a trigger signal. Accordingly, the

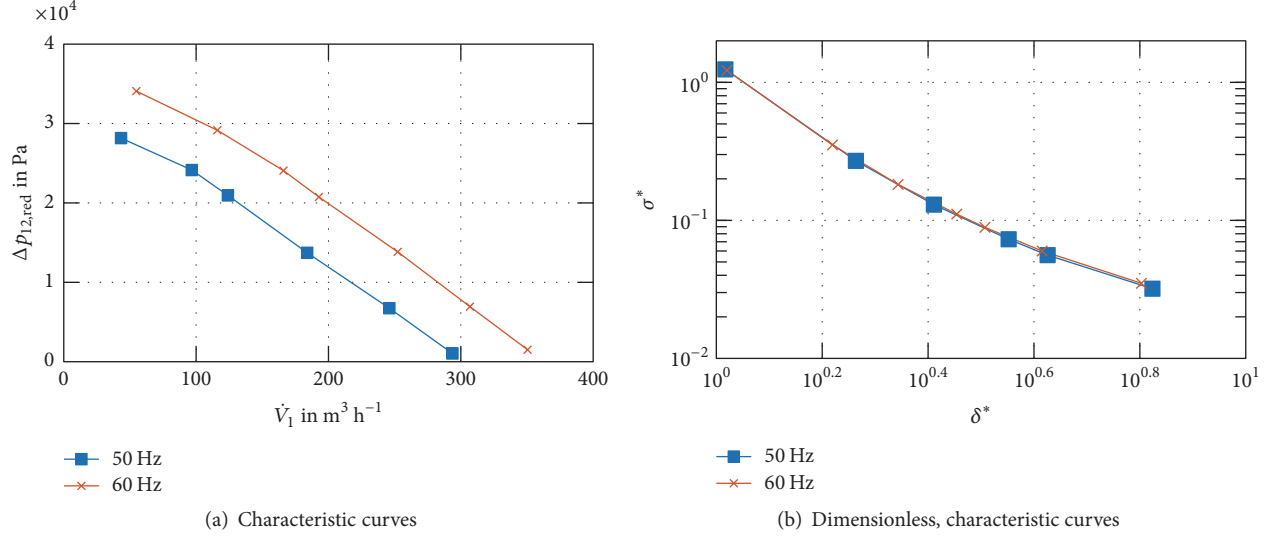


FIGURE 8: Aerodynamic characteristics of the side channel blower under investigation.

systems' temporal offset is in the range of the lowest sampling frequency, that is approx.  $1 \times 10^{-6}$  s.

### 3. Results and Discussion

This section is divided into three parts. In the first part, we present some general characteristics of the side channel blower. The second part includes analyses of the blade surface pressure and the third gives detailed information on the wall pressure inside the side channel.

**3.1. Characteristic Curve.** Side channel blowers feature a nearly linear aerodynamic characteristic curve; see Figure 8(a). For the measured operating points, the flow rate is in a range of  $50 \text{ m}^3 \text{h}^{-1}$  up to  $350 \text{ m}^3 \text{h}^{-1}$  with an inverse pressure range of 35,000 Pa down to 1000 Pa. Higher heads exceed the stall line for the given rotational speeds. The dimensionless characteristic behavior is given in the style of the Cordier-Chart [1] in Figure 8(b) and demonstrates that side channel machines cover the operating range between the classical turbomachines and the displacement pumps.

The pressure measurements on the blade surface and side channel wall were made for the given characteristic curves. A detailed representation of the stripper geometry, which is crucial for a meaningful interpretation of the pressure trends in the following sections, is presented in Figures 9 and 10. The latter represents a radial view of the stripper and contains the important angle  $\theta_{PS,\text{rads}}$  at which the radial closure of a blade segment starts. The former holds two different axial views of the stripper highlighting the start of the axial blade segment closure due to the stripper in the cover  $\theta_{PS,C,\text{axS}}$  and in the housing  $\theta_{PS,H,\text{axS}}$ . Additionally, the cover holds a relaxation groove at the suction side of the stripper to smooth the fluid relaxation that is inherent to the system and caused by the inevitable fluid transport from the pressure to the suction side. The groove begins at  $\theta_{ES}$ . These four basic geometric

angles are referred to in the pressure trends of the blade surface.

**3.2. Blade Surface Pressure.** The blade surface pressure contains information on the pressure rise in the side channel, pressure drop across the stripper, and the change in state of the fluid. These three fundamental processes that describe the typical behavior of side channel blowers. This paper focuses on the first two processes.

The time domain pressure signals on the blade surfaces are given in Figure 11 that is subdivided into suction and pressure side of the blades. The operating point is  $\Delta p_{12,\text{red}} = 14,000 \text{ Pa}$  at 50 Hz rotational speed. As the other operating points show a similar behavior, only the time trends for this one are plotted. The charts resemble the typical pressure rise found in side channel machines. At the beginning of the side channel, where the fluid enters through the suction port at around  $\varphi = 30^\circ$ , the pressure generation is initialized. As the helical flow is not yet existent, only shear stress between impeller and fluid cause an energy transfer and lead to a slight increase of the pressure. Within the first third of the side channel ( $\varphi = 90^\circ$ ), the helical flow has almost completely developed, resulting in a steeper rise of the pressure. The fluid experiences multiple contacts with the impeller until it reaches the end of the side channel. The beginning of the axial stripper in the cover at  $\theta_{PS,C,\text{axS}}$  coincides with the outlet port. The stripper starts at the inner radius of the impeller close to sensor IA2-PS-3 and causes a pressure jump as the fluid is pushed by the decreasing side channel section. As the axial entrance to the blade section decreases, less fluid particles enter the impeller. At the same time the fluid particles in the blade segment are forced to leave in radial direction. This slows down the pressure generation. With the beginning of the radial closure of the blade segment at  $\theta_{PS,\text{rads}}$  and its finalization approx.  $7^\circ$  later, the fluid is abruptly enclosed in-between two blades and the stripper causes a pressure shock, i.e., the sudden rise of the local pressure due to abrupt

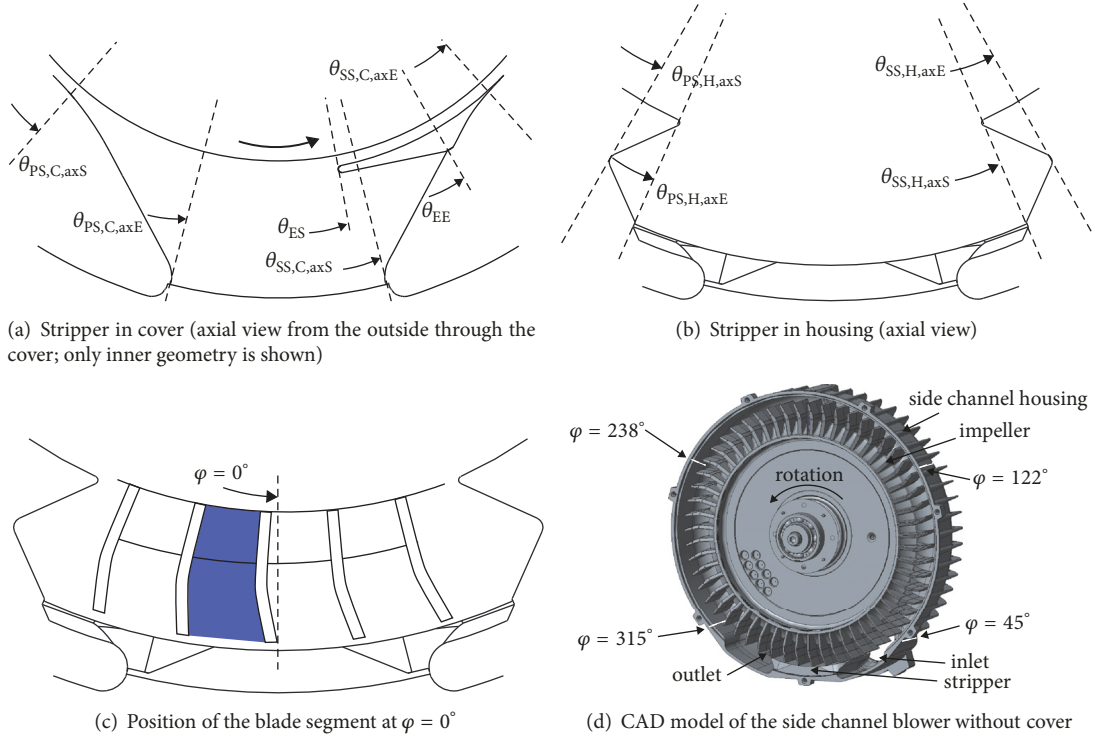


FIGURE 9: Stripper geometry,  $0^\circ$ -position of blade segment and CAD model of the opened side channel blower.

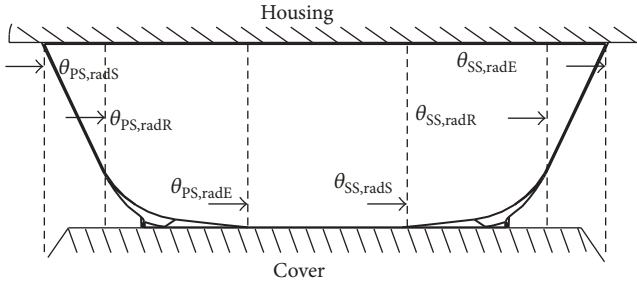


FIGURE 10: Radial stripper (view in positive radial direction).

geometric changes. After the radial movement of the fluid has stopped, the pressure shock diminishes. From a technical point of view, the clearance between the moving blades and the stationary stripper has to be finite. In case of the side channel blower under investigation, it is between  $0.4 \cdots 0.5$  mm. The fluid between the blades starts relaxing to the suction side due to this clearance. For small pressure differences, the relaxation allows for a complete equalization with the suction side pressure. For higher pressure differences, an additional relaxation groove has been implemented into the stripper in the cover. This groove starts at  $\theta_{ES}$ , increases the flow cross section, and results in a faster pressure adjustment. On the suction side, the inertia of the relaxing fluid causes a negative pressure shock. Then, the pressure generation restarts.

A part of the fluid is always transported along the stripper from the pressure side to the suction side because of the mechanical construction. While this volume flow is

constant, defined by the volume of the blade segments and the rotational speed, the transported mass depends on the working point and, consequently, on the fluid density.

The difference between the pressure side of the blade (Figure 11(a)) and the suction side (Figure 11(b)) can mainly be found in slightly higher pressure values during the blade segment passage through the side channel. Additionally, while passing the stripper, the pressure shocks double their amplitude from the suction side of the blade to its pressure side. For the actual working point of  $\Delta p_{12,red} = 14$  kPa, the pressure shocks on the pressure side of the blades are in a range of 3000 Pa compared to the suction side with 1500 Pa.

The pressure distribution is shown in a sensor-averaged and phase-locked ensemble-averaged type for different working points and rotational speeds in Figure 12. At a rotational speed of 50 Hz, 1500 periods, and at a rotational speed of 60 Hz, 1800 periods were averaged since the measurement time was 30 s. The operating point logically influences the pressure gradient, but as the different trends show, the gradient itself changes along the side channel. While low integral pressure differences of up to around  $0.3 \cdot \Delta p_{12,red,max}$ , i.e. 9000 Pa at 50 Hz rotational speed, hold a nearly constant pressure gradient, an increasing integral pressure difference leads to an additional rise. All measurements inhibit a pressure drop at around  $180^\circ$  that is caused by a small rib on the inner wall of the side channel. Different rotational speeds mainly have an impact on pressure relaxation, i.e., the decrease of the pressure due to expansion of the enclosed (blade segment) volume, in the area of the stripper. The higher the rotational speed, the less the time available to the fluid to

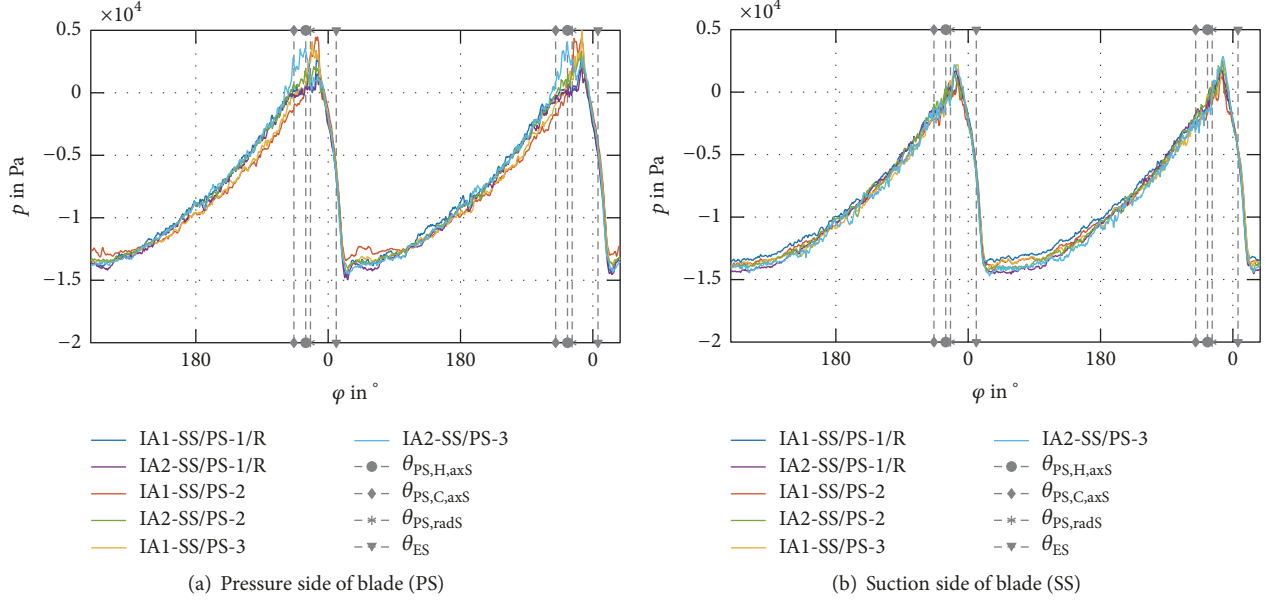


FIGURE 11: Time trend of pressure signal on the blade surface at a rotational speed of  $f = 50$  Hz and a pressure difference  $\Delta p_{12,\text{red}} = 14,000$  Pa. Note. Configuration IAx-PS-1 is not shown.

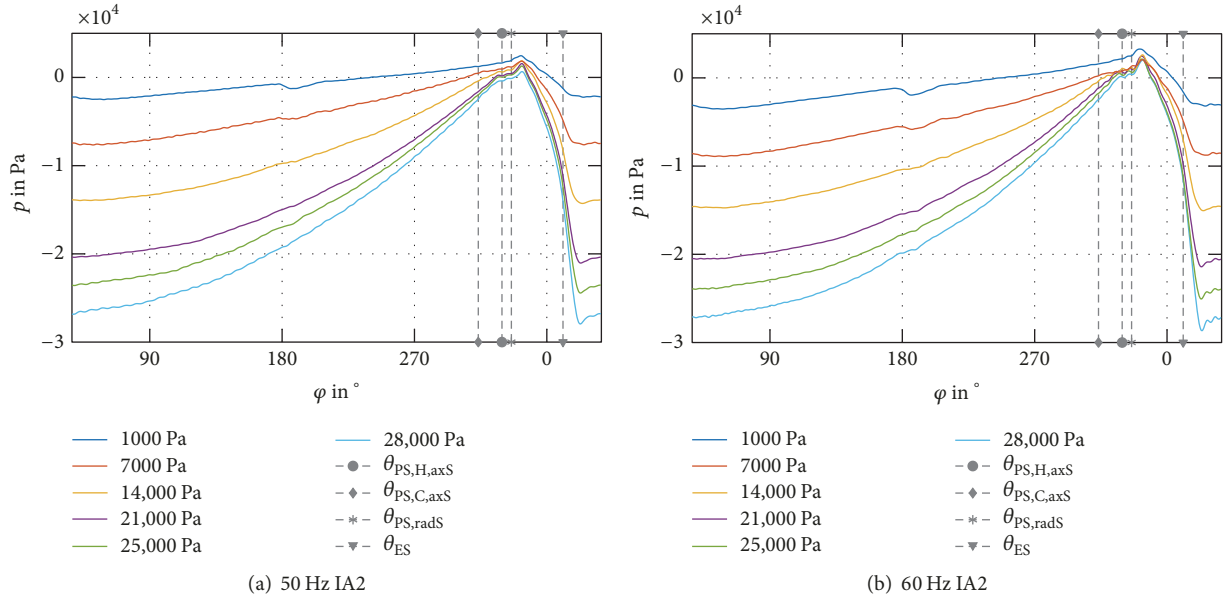


FIGURE 12: Sensor-averaged and phase-locked ensemble-averaged pressure on the blade surface for different operating points  $\Delta p_{12,\text{red}}$  and rotational speeds.

relax to the suction side while being transported along the stripper. Hence, the pressure decrease up to the beginning of the relaxation groove slows down and the relaxation process through the relaxation groove intensifies. This results in higher flow speeds and accordingly in stronger oscillations at the suction side of the stripper beginning from  $\varphi = 0^\circ$ . In summary, faster geometric changes as seen by the rotating blade segment increase the pressure fluctuations and induce a stronger turbulence in the flow field.

The fluctuations of the pressure signal were evaluated as the standard deviation for each rotational position. Figure 13 holds the corresponding trends for both rotational speeds. The fluctuations rise in circumferential direction. An increase of the integral pressure difference results in higher fluctuations. This increase covers the fluctuations at  $200^\circ$  induced by the rib and explains why the phenomenon cannot be identified at higher integral pressure differences (see Figure 12). The trends also show that the fluctuations are

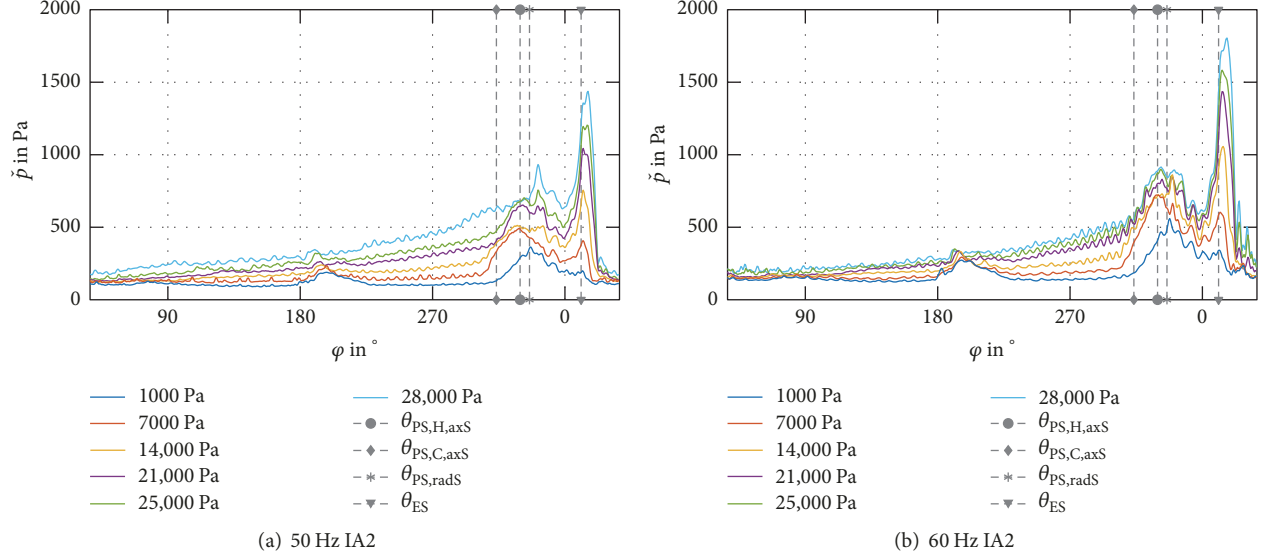


FIGURE 13: Standard deviation of pressure  $\tilde{p}$  on the blade surface for impeller arrangement 2 (IA2).

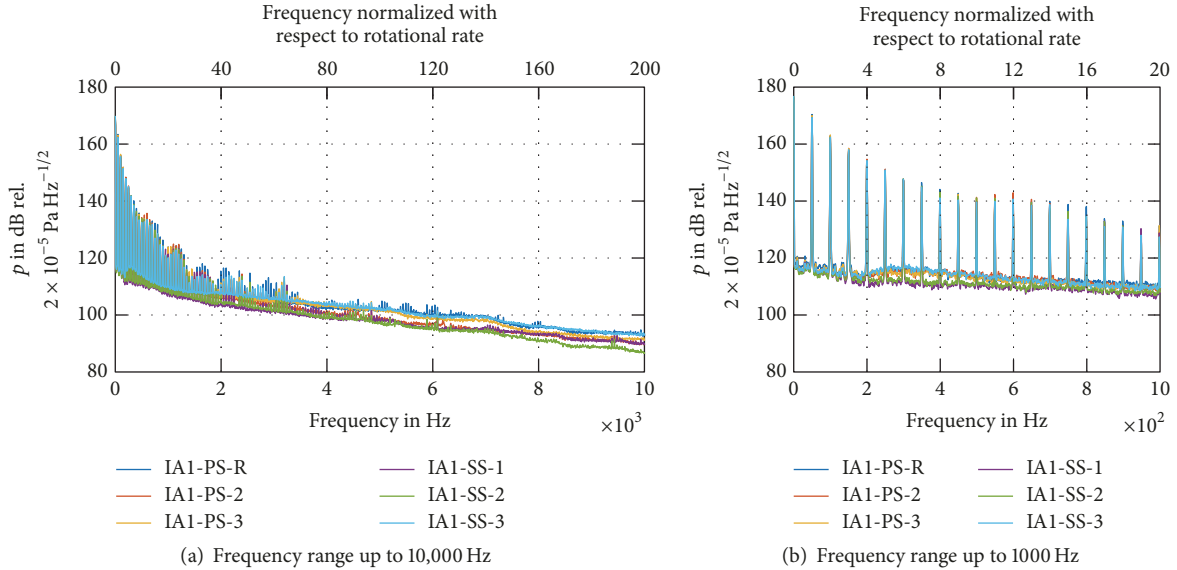


FIGURE 14: PSD of blade surface pressure at a rotational speed of  $f = 50$  Hz and operating point  $\Delta p_{12,\text{red}} = 28,000$  Pa.

located at fixed positions as periodic oscillations occur along the side channel, especially in the range of  $\varphi = 200 \dots 300^\circ$ . For varying circumferential positions, the spatial averaging process suppresses such oscillations. When entering the stripper, the fluctuations abruptly increase as the flow field is disturbed. During the carry-over, the fluid is enclosed in the blade segment and, accordingly, the fluctuations decrease. The strongest variations in the pressure field are induced by the relaxation process on the suction side of the stripper starting from  $\theta_{\text{ES}}$ . At low pressure differences, the pressure side fluctuations predominate slightly, the suction side fluctuations are stronger for pressure differences higher

than  $0.3 \cdot \Delta p_{12,\text{red},\max}$ . As the trends proof, the stripper is the main source for pressure fluctuations in side channel blowers.

The power spectral density (PSD) in Figure 14 for  $\Delta p_{12,\text{red}} = 28,000$  Pa identifies the rotational speed of 50 Hz and its harmonics as dominant frequency components in the pressure signal. The spectra are only shown for impeller arrangement 1 as the other sensor positions represent a similarly behavior. The highest peaks are the mean offset at 0 Hz followed by the peak at the rotational speed. The harmonics decrease until approx. 3 kHz and vanish in the noise floor that starts at 120 dB and drops constantly to 90 dB at 10 kHz. The effects at the rotational speed in the rotating

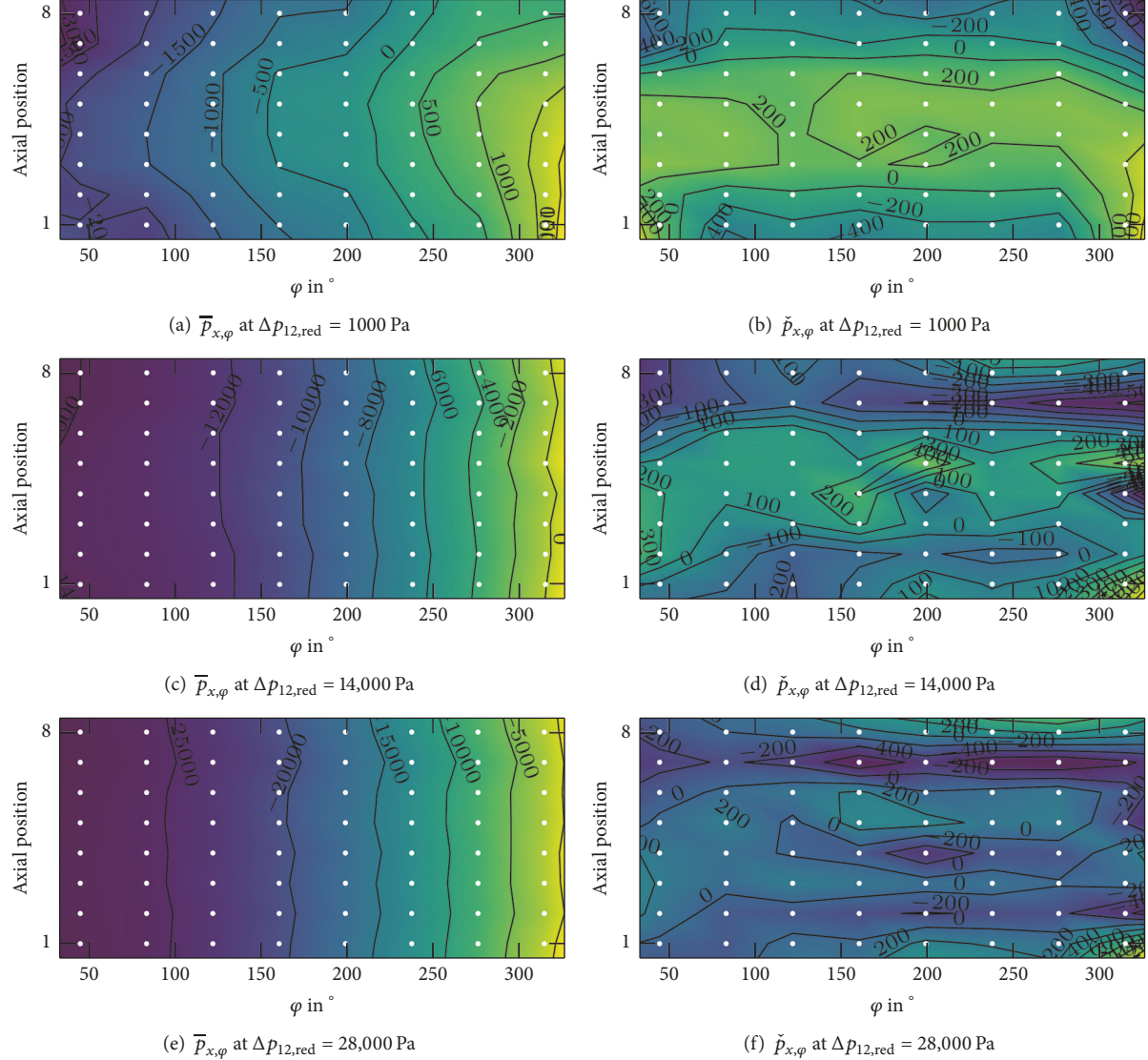


FIGURE 15: Wall pressure distribution at a rotational speed of 50 Hz for different operating points. (a, c, e) Static pressure relative to ambient pressure  $\bar{p}_{x,\varphi}$ . (b, d, f) Local mean value-adjusted static pressure relative to ambient pressure  $\check{p}_{x,\varphi}$  according to equation (6).

system, i.e., on the blade surface, occur at the blade passing frequency in the stationary system, i.e., on the side channel housing. Other temporal effects than the blade segment passage through the circumferentially increasing pressure field cannot be identified.

**3.3. Wall Pressure.** While the pressure on the blade surfaces changes along the path of the fluid particles in the side channel according to the pressure difference between inlet and outlet, the pressure sensors on the wall are exposed to a nearly constant pressure field that is influenced by minor fluctuations. The time-averaged contour plots of the pressure on the side channel wall are depicted in Figures 15(a), 15(c), and 15(e) with the measurement positions marked as white dots. The color scale is just for illustration and changes for each subplot; hence absolute values are provided by the contour lines. As the scale over the whole pressure range

suppresses the visualization of local variations in the pressure field, the local circumferential mean value-adjusted static pressure is plotted in the right column of the same figure. It is calculated as follows:

$$\check{p}_{x,\varphi} = \bar{p}_{x,\varphi} - \bar{p}_\varphi. \quad (6)$$

According to this equation, the local circumferential mean value  $\bar{p}_\varphi$  holds all sensors at the same circumferential position  $\varphi$  and is subtracted from each pressure trend at the same  $\varphi$ .

The mean wall pressure distribution for three exemplary working points, shown in Figure 15, confirms the findings from the previous pressure measurements on the blade surface: the pressure gradient in circumferential direction increases in correlation with the pressure difference  $\Delta p_{12,\text{red}}$ . The double-flow setup of the side channel induces an almost plane-symmetric pressure field with the axial plane between

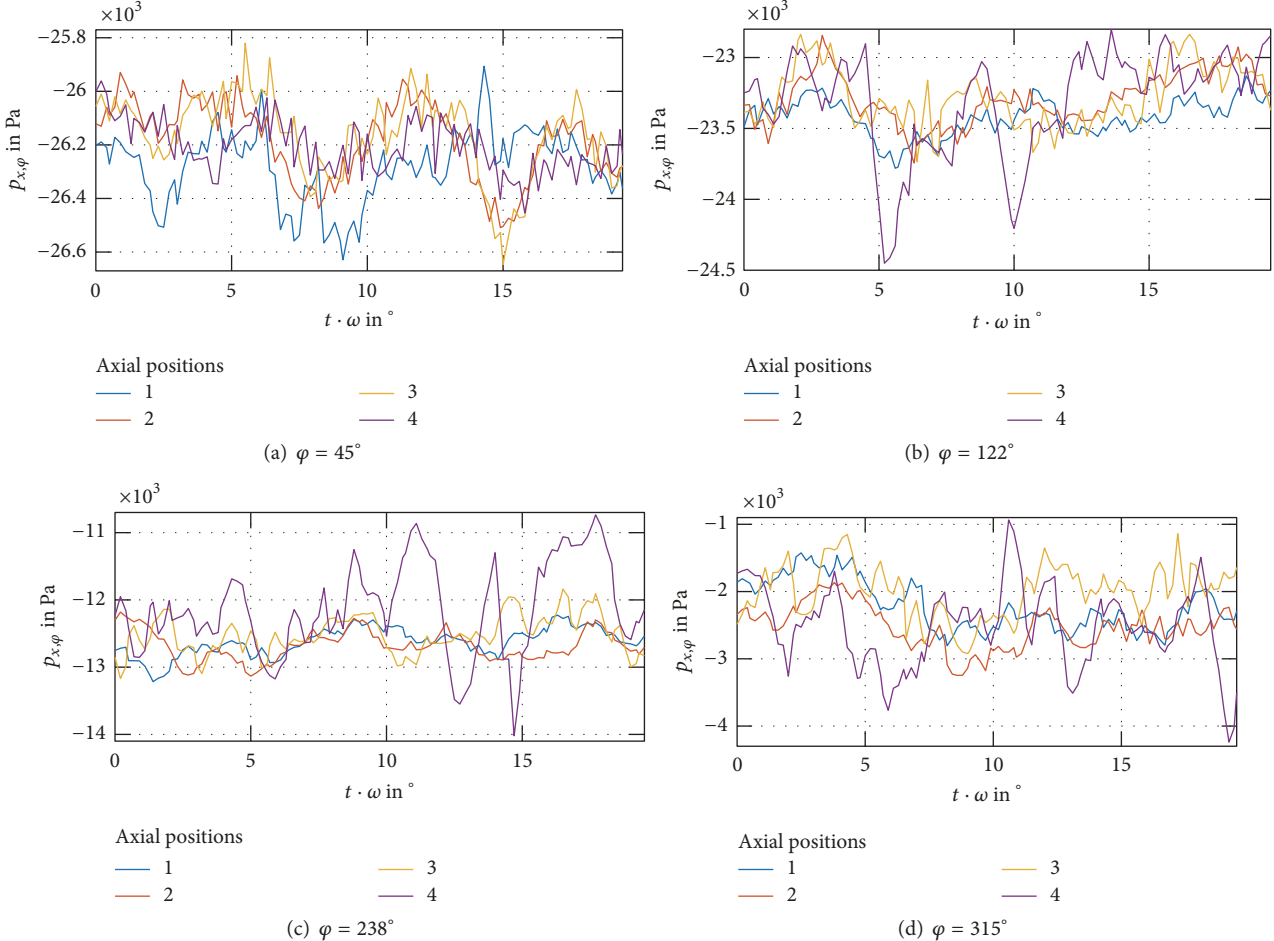


FIGURE 16: Pressure at a rotational speed of 50 Hz and  $\Delta p_{12,\text{red}} = 28,000$  Pa measured at the unsteady measurement positions. The term  $t \cdot \omega$  was chosen instead of  $\varphi$  to describe the rotation of the impeller.

axial positions 4 and 5, i.e., the middle of the impeller. Slight asymmetries occur near the inlet and outlet for outer axial positions caused by the asymmetric geometry. Axial position 8 at the inlet holds the lowest pressure values for all working points because it is closest to the inlet port. At the same circumferential position at axial positions 6 to 8, the pressure is generally increased as the fluid carried over expands in these directions. This issue is depicted in the local mean value-adjusted  $\check{p}_{x,\varphi}$  contour plots. Along the side channel, both flows behave similarly. The pressure at the radial side channel wall, axial positions 3 to 6, is affected by the circulatory flow and its deflection from a radial to the axial direction. This effect forms a local stagnation area and rise in pressure. Near the outlet, the fluid from the flow in the cover is forced to change its direction to leave the side channel through the outlet port. This geometric restriction induces a local stagnation pressure at the end of the side channel ( $\varphi > 300^\circ$ ) near axial position 1. It is additionally intensified by the abrupt occurrence of the stripper. In contrast to this, axial positions 6 to 8 are exposed to a local pressure drop as fluid of both flows passes these positions and induces a

local rise of the flow velocity. Different working points and rotational speeds create similar pressure fields.

The time trends for one flow (axial positions 1–4) of the double-flow configuration are presented in a temporally resolved form in Figure 16 for a pressure difference of  $\Delta p_{12,\text{red}} = 28,000$  Pa at four different circumferential positions. The trends represent three blade passages, i.e., an impeller rotation of  $19.4^\circ$ . The rotation of the impeller induces a periodical fluctuation of the measured pressure, especially close to the inlet port at  $\varphi = 45^\circ$ , where the circular flow is not yet established, the blade passage has a clear impact. For the other three circumferential positions, the stochastic pressure fluctuations increase, as the flow field becomes more and more turbulent with the initialization of the circular flow. The pressure sensor in the radial side channel wall (axial position 4) is subject to the highest fluctuations as it is exposed to the radial jet of the circular flow. From the inlet port to the outlet port, the fluctuations increase approx. by a factor of four.

Despite the increasing turbulence, the wall pressure field is still dominated by the periodical passage of the blades as shown by the phase-locked ensemble-averaged wall pressure

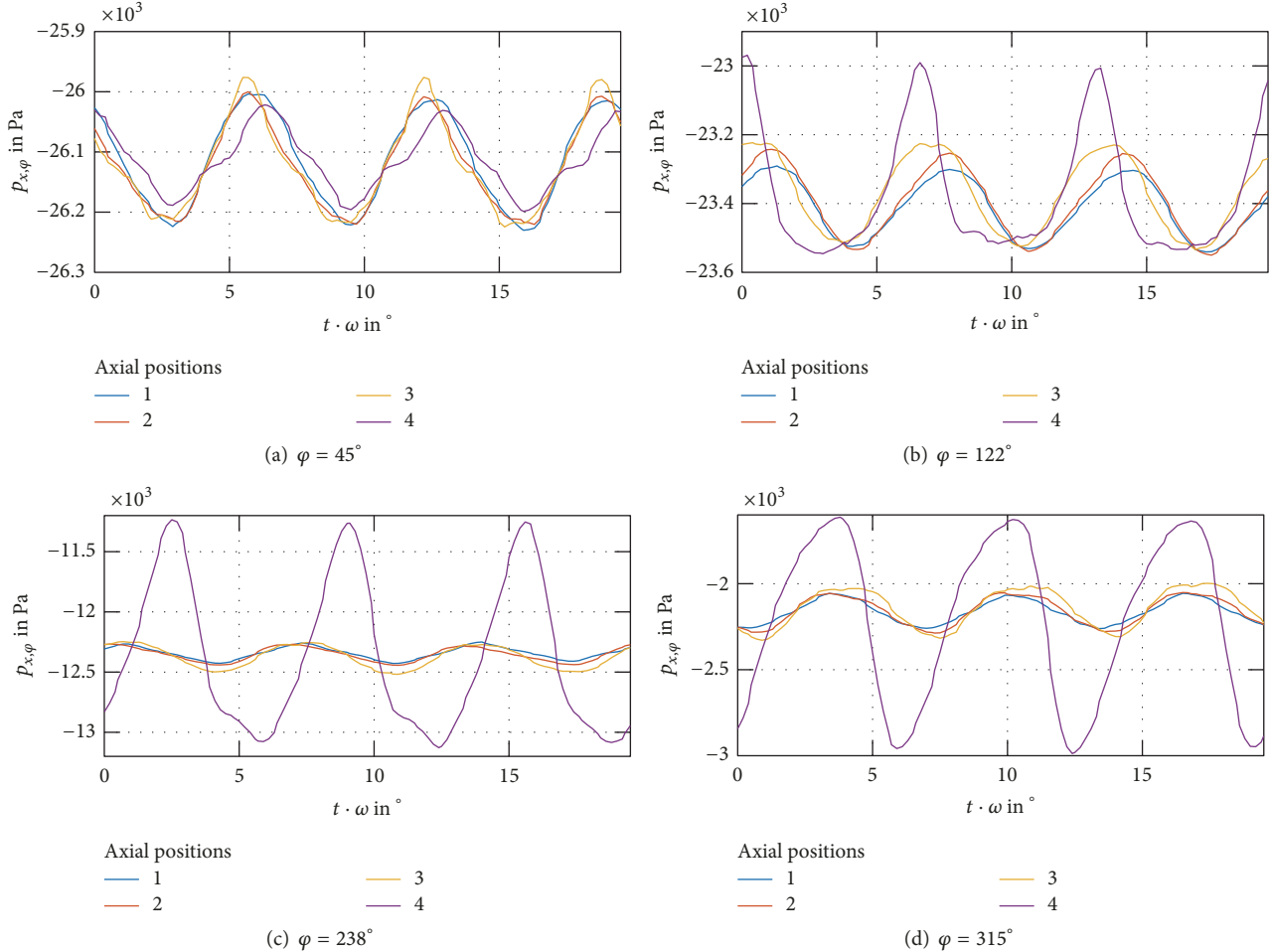


FIGURE 17: Phase-locked ensemble-averaged wall pressure for four different axial and circumferential positions at a rotational speed of 50 Hz and  $\Delta p_{12,\text{red}} = 28,217 \text{ Pa}$  measured at the unsteady measurement positions. Each subfigure holds the plots for four different axial positions at the same circumferential position according to Figure 7. The term  $t \cdot \omega$  was chosen instead of  $\varphi$  to clarify the rotation of the impeller.

in Figure 17. The periodic fluctuations on the radial side channel wall increase in circumferential direction while the axial side channel (axial positions 1 to 3) remains nearly unaffected. At the inlet port, the fluctuations have amplitudes of 200 Pa and rise up to 2500 Pa at the outlet port for the axial position 4. The rise of periodic fluctuations on the radial wall can be explained by the development of the circulatory flow in circumferential ( $\varphi$ ) direction as already proven by the nonconstant pressure gradient. An increase of the energy transfer from the impeller to the fluid is induced by a greater circulatory flow speed as more blade passages occur. This circulatory flow is perpendicular to the main flow in circumferential direction. Hence, the stagnation pressure due to the flow deflection on the radial wall increases. Additionally, the pulse duty factor of the oscillations elevates in circumferential direction. This indicates that more fluid is circulating through the blade segment by means of a better usage of the blade segment cross section by an even velocity distribution. As the circulating mass flow increases, more energy can be transferred from the impeller to the fluid.

The spatially resolved wall pressure fluctuations are shown as the standard deviation in Figure 18. These contour plots confirm four facts found from the previous evaluations: firstly, the pressure fluctuations with the highest amplitudes are located on the radial side channel wall. Secondly, the fluctuations increase in circumferential direction. Thirdly, the amplitudes of the fluctuations correlate with the pressure difference  $\Delta p_{12,\text{red}}$ . Fourthly, the double-flow configuration induces a nearly symmetric flow field except for the area close to inlet and outlet port.

A PSD of the wall pressure signal in Figure 19 identifies the blade passage at the blade passing frequency ( $f_{\text{bpf}} = 55 \cdot 50 \text{ Hz} = 2750 \text{ Hz}$ ) and its harmonics as dominant peaks in the spectra. The given spectra for three different axial positions, namely, 1, 4, and 6, are plotted for four different circumferential positions. They affirm that the fluctuations as well as the stochastic noise floor in the pressure field rise in circumferential direction. In addition to the peaks at  $f_{\text{bpf}}$  and multiples of it, an increased broadband noise in the frequency range up to approx. 400 Hz is detected,

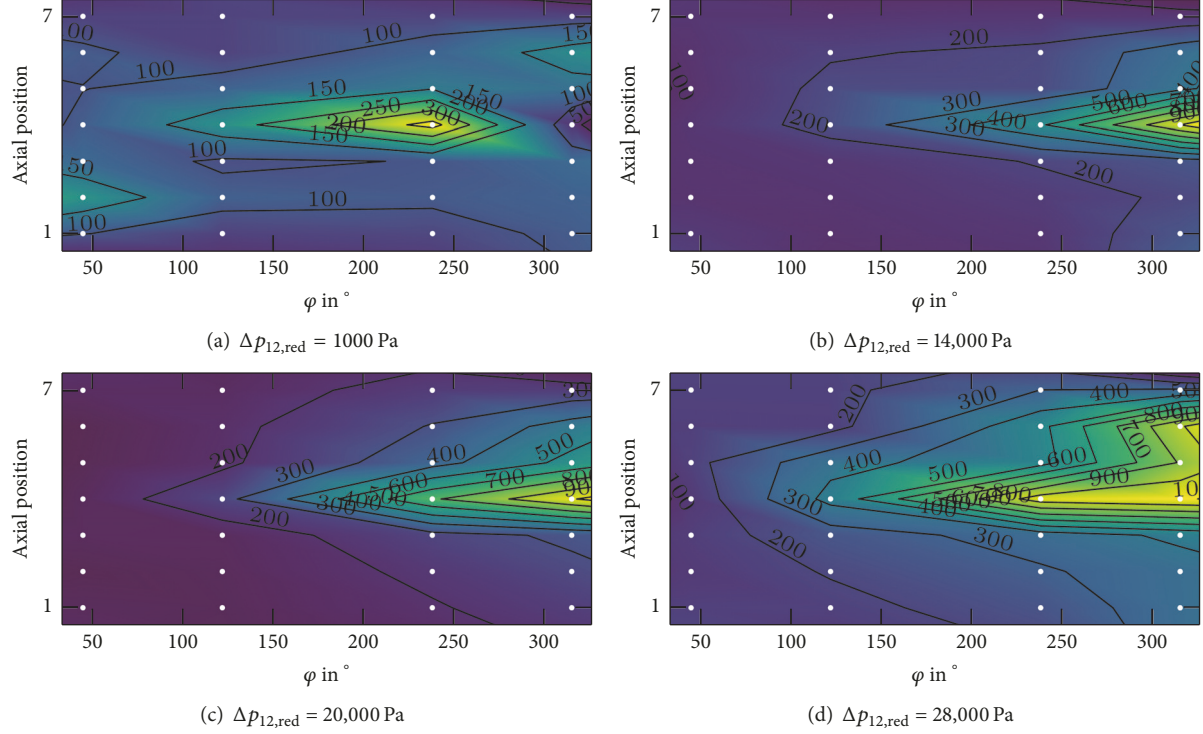


FIGURE 18: Standard deviation of wall pressure  $\check{P}_{x,\varphi}$  at a rotational speed of  $f = 50$  Hz for four different operating points.

especially at the rotational speed of 50 Hz. At the rotational speed, rigid body motions occur due to the imbalance of the impeller. This induces pressure oscillations on the surface of the rigid body, i.e., the side channel housing. The axial unsteady measurement positions that are located closest to the impeller in upstream and downstream direction of the circulatory flow are axial positions 1 and 4. They are exposed to a higher noise floor and higher peaks than those positions that are located further away in streamwise direction of the circulatory flow, such as axial position 6.

#### 4. Conclusions

In this work, the pressure field of a side channel blower was analyzed by unsteady measurements on the blade surface and on the side channel wall. Both setups yielded detailed information on the spatial and temporal behavior of the flow field. The main findings can be summarized as follows:

- (i) The pressure field in a blade segment and on the side channel wall features similar effects. These effects concur in the temporal as well as the spatial domain.
- (ii) The pressure gradient in circumferential direction is not constant. Especially at high pressure differences, the gradient increases in circumferential direction.
- (iii) In combination with the former finding, it was shown that the circulatory flow field initializes within in the first approx.  $90^\circ$  of the side channel. Additionally, the efficiency of the circulatory flow, by means of momentum transfer from the impeller to fluid, improves in circumferential direction. Hence, an optimized inlet port improves the initialization of the circulatory flow and, accordingly, the pressure rise.
- (iv) The pressure field on the side channel wall is dominated by fluctuations at the blade passing frequency and on the blade surface by the rotational speed. The latter is caused by the passage of the blade segment over the stripper, whereas the former is induced by the radial jet of the circulatory flow being deflected by the radial side channel wall.
- (v) The amplitude of the pressure fluctuations correlates with the integral pressure difference  $\Delta p_{12,\text{red}}$ .
- (vi) The asymmetric setup of inlet and outlet port with reference to the double-flow configuration forces the fluid in the flow away from the ports to abrupt changes in the flow direction. That in turn causes high pressure fluctuations near the stripper. Correspondingly, a symmetric setup for both ports leads to a smooth deflection of the fluid in case of a double-flow configuration.
- (vii) The closing of the blade segment by the stripper induces pressure shocks and the opening on the suction side results in additional oscillations due to the mass inertia of the expanding fluid.
- (viii) The pressure relaxation starts directly after the closure of the blade segment is completed. A higher rotational

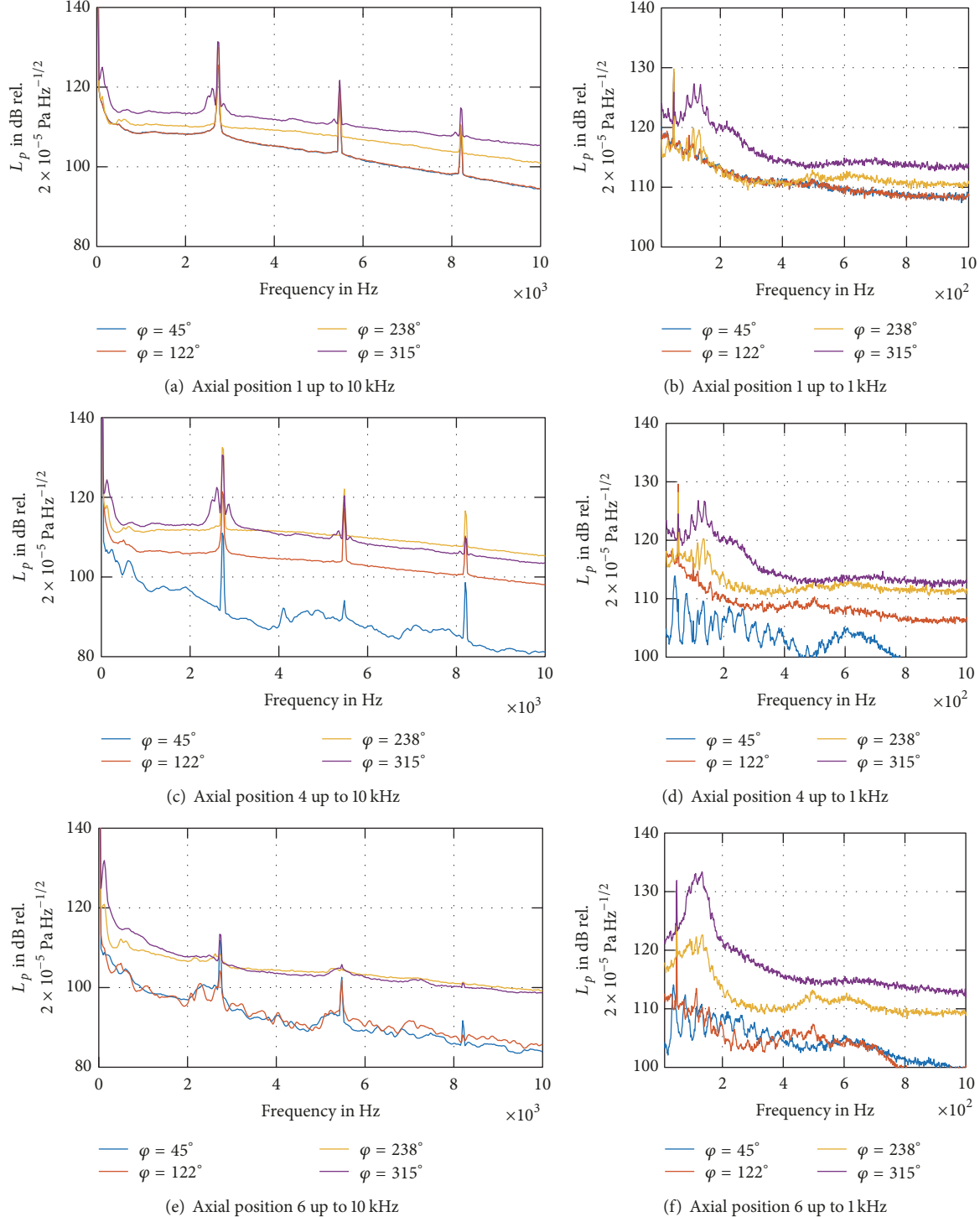


FIGURE 19: PSD of wall pressure at a rotational speed of 50 Hz and  $\Delta p_{12,\text{red}} = 28,000 \text{ Pa}$ . Each plot contains the same axial position for different circumferential positions.

speed leads to less relaxation through the small gap between blade and stripper and, hence, causes a stronger relaxation at beginning of the relaxation groove.

The pressure field in side channel blowers is complex and influenced by many factors. A geometric adaption for a faster

initialization of the circulatory flow improves the pressure generation and the characteristic curve of the turbomachine.

## Nomenclature

- $\delta^*$ : Diameter number
- $\eta$ : Efficiency

$\omega$ :	Angular velocity
$\psi^*$ :	Pressure coefficient
$\varphi^*$ :	Flow coefficient
$x$ :	Axial position
$\varphi$ :	Azimuth; circumferential position
$\sigma^*$ :	Tip speed ratios
$A_p$ :	Pipe cross-sectional area
$\bar{c}_C$ :	Average velocity of the fluid in circumferential direction
$n$ :	Polytropic exponent
$p_1$ :	Static inlet pressure
$p_2$ :	Static outlet pressure
$\bar{p}_\varphi$ :	Averaged static pressure relative to ambient pressure for all axial measurement positions at $\varphi$ $(= (1/N) \sum_{x=1}^N \bar{p}_{x,\varphi})$
$\bar{P}_{x,\varphi}$ :	Mean static pressure relative to ambient pressure at location $(x, \varphi)$
$\check{p}_{x,\varphi}$ :	Local mean value-adjusted static pressure relative to ambient pressure
$p_{sc}$ :	Atmospheric pressure for standard conditions
$R_s$ :	Specific gas constant for air
$T_1$ :	Inlet temperature
$T_2$ :	Outlet temperature
$T_{sc}$ :	Atmospheric temperature for standard conditions
$u$ :	Rotational velocity
$\dot{V}_1$ :	Inlet volume flow
$Y_p$ :	Specific polytropic work.

## Conflicts of Interest

The authors declare that they have no conflicts of interest.

## Acknowledgments

The authors gratefully acknowledge the support from the Green Factory Bavaria and Gardner Denver Deutschland GmbH. Furthermore, they thank Till Heinemann and Alexander Lodermeyer.

## References

- [1] G. H. Grabow, "Das erweiterte "Cordier"-Diagramm für Fluidenergiemaschinen und Verbrennungsmotoren," *Forschung im Ingenieurwesen*, vol. 59, no. 3, pp. 42–50, 1993.
- [2] D. Surek, "Turbulente Wirbelströmung und dynamische Druckschwankungen in Seitenkanalmaschinen," *Forschung im Ingenieurwesen*, vol. 63, no. 4, pp. 85–101, 1997.
- [3] D. Surek, "Strömungsvorgänge und Schwingungen in Seitenkanalverdichtern, Beiträge zu Fluidenergiemaschinen," *Faragallah*, 2000.
- [4] H. Engels, *Untersuchungen an Ringpumpen (Seitenkanalpumpen)* [PhD thesis], TH Hannover, 1940.
- [5] W. Wilson, M. Santalo, and J. Oelrich, "A theory of the fluid-dynamic mechanism of regenerative pumps," *Transactions of the ASME*, vol. 77, pp. 1303–1311, 1955.
- [6] Y. Senoo, "Researches on peripheral pumps," in *Reports of Research Institute for Applied Mechanics*, vol. 3, pp. 53–113, 1954.
- [7] M. Shimosaka, "Research on the characteristics of regenerative pump: 2nd report, theoretical research on the performance," *Bulletin of JSME*, vol. 3, no. 10, pp. 191–199, 1960.
- [8] H. Sixsmith and H. Altmann, "A regenerative compressor," *Journal of Engineering for Industry*, vol. 99, no. 3, pp. 637–647, 1977.
- [9] J. W. Hollenberg and J. H. Potter, "An investigation of regenerative blowers and pumps," *Journal of Engineering for Industry*, vol. 101, no. 2, pp. 147–152, 1979.
- [10] D. N. D N Andrew, "The calculation of flow in regenerative turbomachines by a streamline curvature method," *Proceedings of the Institution of Mechanical Engineers, Part A: Journal of Power and Energy*, vol. 204, no. 2, pp. 121–129, 1990.
- [11] G. H. Grabow and N. D. Suong, "Berechnungsmodell zur Auslegung von Seitenkanalmaschinen," *Forschung im Ingenieurwesen*, vol. 58, no. 11–12, pp. 273–282, 1992.
- [12] T. Meakhail and S. O. Park, "An improved theory for regenerative pump performance," *Proceedings of the Institution of Mechanical Engineers, Part A: Journal of Power and Energy*, vol. 219, no. 3, pp. 213–222, 2005.
- [13] F. J. Quail, M. Stickland, and A. Baumgartner, "A one-dimensional numerical model for the momentum exchange in regenerative pumps," *Journal of Engineering for Gas Turbines and Power*, vol. 133, no. 9, Article ID 093001, 2011.
- [14] F. J. Quail, T. H. Scanlon, and A. Baumgartner, "Design study of a regenerative pump using one-dimensional and three-dimensional numerical techniques," *European Journal of Mechanics - B/Fluids*, vol. 31, no. 1, pp. 181–187, 2012.
- [15] I. S. Yoo, M. R. Park, and M. K. Chung, "Improved momentum exchange theory for incompressible regenerative turbomachines," *Proceedings of the Institution of Mechanical Engineers, Part A: Journal of Power and Energy*, vol. 219, no. 7, Article ID A09704, pp. 567–581, 2005.
- [16] J. W. Song, M. Raheel, and A. Engeda, "A compressible flow theory for regenerative compressors with aerofoil blades," *Proceedings of the Institution of Mechanical Engineers, Part C: Journal of Mechanical Engineering Science*, vol. 217, no. 11, pp. 1241–1257, 2003, <http://pic.sagepub.com/cgi/content/abstract/217/11/1241>.
- [17] Y. Senoo, "Theoretical research on friction pump," *Institute of Fluid Engineering*, vol. 5, pp. 23–48, 1948.
- [18] H. Iversen, "Performance of the periphery pump," in *Trans. ASME*, vol. 77, pp. 19–28, 1955.
- [19] F. S. Weinig, "Analysis of traction pumps," *Hydraulic Devison of the ASME*, 1955.
- [20] S. Münsterjohann, T. Heinemann, and S. Becker, "Circulatory flow characteristics in side channel blowers," *Applied Mechanics and Materials*, vol. 871, pp. 237–243, 2017.
- [21] J. Beilke, *Numerische Untersuchungen zur instationären Strömung in Seitenkanalverdichtern* [PhD thesis], Technische Universität Bergakademie, Freiberg, Germany, 2005.
- [22] V. Weise and J. Beilke, "Akustische Untersuchungen zur Verminderung der Schallabstrahlung bei der Energieübertragung in Seitenkanalmaschinen," in *DFG-Forschungsbericht*, TU Bergakademie, Freiberg, Germany, 1997.
- [23] A. Fleder and M. Böhle, "A systematical study of the influence of blade length, blade width, and side channel height on the performance of a side channel pump," *Journal of Fluids Engineering*, vol. 137, no. 12, Article ID 121102, 2015.

- [24] N. D. Karlsen-Davies and G. A. Aggidis, "Regenerative liquid ring pumps review and advances on design and performance," *Applied Energy*, vol. 164, pp. 815–825, 2016.
- [25] D. Surek, "Überschallströmung und instationäre Verdichtungsstöße in Seitenkanalverdichtern," *Forschung im Ingenieurwesen*, vol. 74, no. 2, pp. 63–76, 2010.
- [26] D. Surek, "Druckverlauf und Gasdruckschwingung im Schaufelkanal von Seitenkanalverdichtern," *Forschung im Ingenieurwesen*, vol. 75, no. 3, pp. 139–152, 2011.
- [27] T. Grohmann, *Lokalisierung und Klassifizierung tonaler Schallquellen in Seitenkanalgebläsen*, 9, Shaker Verlag, 2010.

